

High-Temperature Ultrafast Sintering: Exploiting a New Kinetic Region to Fabricate Porous Solid-State Electrolyte Scaffolds

Ruiliu Wang, Qi Dong, Chengwei Wang, Min Hong, Jinlong Gao, Hua Xie, Miao Guo, Weiwei Ping, Xizheng Wang, Shuaiming He, Jian Luo, and Liangbing Hu*

Solid-state batteries (SSBs) promise better safety and potentially higher energy density than the conventional liquid- or gel-based ones. In practice, the implementation of SSBs often necessitates 3D porous scaffolds made by ceramic solid-state electrolytes (SSEs). Herein, a general and facile method to sinter 3D porous scaffolds with a range of ceramic SSEs on various substrates at **high temperature in seconds** is reported. **The high temperature enables rapid reactive sintering toward the desired crystalline phase and expedites the surface diffusion of grains for neck growth; meanwhile, the short sintering duration limits the coarsening, thus accurately controlling the degree of densification to preserve desired porous structures, as well as reducing the loss of volatile elements.** As a proof-of-concept, a composite SSE with a good ionic conductivity (i.e., $\approx 1.9 \times 10^{-4} \text{ S cm}^{-1}$ at room temperature) is demonstrated by integrating poly(ethylene oxide) with the 3D porous $\text{Li}_{6.5}\text{La}_3\text{Zr}_{1.5}\text{Ta}_{0.5}\text{O}_{12}$ scaffold sintered by this method. This method opens a new door toward sintering a variety of ceramic-SSE-based 3D scaffolds for all-solid-state battery applications.

1. Introduction

Li-ion and Li-metal batteries are indispensable in modern society for portable electronic devices, electrical vehicles, and grid-scale energy storage facilities.^[1–4] However, their safety

issue has greatly hindered the development of these technologies for broader applications.^[5,6] Solid-state electrolytes (SSEs) represent one promising solution to this problem as they offer better safety and potentially higher volumetric energy density.^[7–11] A range of SSEs materials have been explored so far, with polymers^[12,13] and ceramic Li-ion conductors^[14] being the leading contenders. Among them, polymer SSEs show seamless interfacial contact and relatively larger production scale,^[15] but suffer from low mechanical strength^[16] and poor thermal stability. In addition, the organic backbone of these materials does not fundamentally address the flammability issue and is prone to thermal runaway. In comparison, ceramic Li-ion conductors such as garnet,^[17,18] LISICON $\text{Li}_{10}\text{GeP}_2\text{S}_{12}$,^[19] and so on exhibit better mechanical strength and Li-ion conductivity, but comes with


an expense of processability, poor interfacial contact, and flexibility.^[20,21] Despite the high promise and broad research interest, these problems continue to limit the practicality of ceramic SSEs for broader applications.^[22,23] It has been shown that integrating ceramic and polymer SSEs together promises a viable route to harvest the merits of the two while neutralizing each other's drawbacks.^[6,24–26] Such a “polymer in ceramic” strategy often requires the synthesis of 3D porous ceramic scaffold to form continuous Li-ion transport pathways with polymer SSEs.^[27–29] On the other hand, the porous ceramic scaffold can also be used to decrease the interfacial resistance between the electrolyte and Li metal anode,^[30] conventional intercalation cathode,^[31] or conversion cathode such as sulfur.^[32,33]

To achieve desired porous structure with a pure crystalline phase, conventional sintering methods typically rely on pore-forming agent^[32] or freeze casting.^[29,34,35] In particular, these conventional approaches to sinter porous ceramics can take advantage of prolonged sintering time at relatively low temperatures. In this low-temperature kinetic region, surface diffusion, which has a low activation energy, controls and leads to neck forming (bonding) without densification, yet surface diffusion also promotes grain growth (coarsening). The long sintering time also causes significant Li loss due to its highly volatile nature, which deteriorates the quality of the porous

R. Wang, Dr. Q. Dong, Dr. C. Wang, M. Hong, J. Gao, Dr. H. Xie, M. Guo, W. Ping, Dr. X. Wang, Dr. S. He, Prof. L. Hu
 Department of Materials Science and Engineering
 University of Maryland
 College Park, MD 20742, USA
 E-mail: binghu@umd.edu

Prof. J. Luo
 Department of NanoEngineering
 Program of Materials Science and Engineering
 University of California, San Diego
 La Jolla, CA 92093, USA

Prof. L. Hu
 Center for Materials Innovation
 University of Maryland
 College Park, MD 20742, USA

 The ORCID identification number(s) for the author(s) of this article can be found under <https://doi.org/10.1002/adma.202100726>.

DOI: 10.1002/adma.202100726

SSEs. Herein, we report a new method to synthesize 3D porous ceramic SSE scaffolds at high temperature in seconds.^[36] In our approach, the solid-state reaction along with bulk and grain boundary diffusion would result in high densification rates, but we limit the total densification via precisely control the sintering process only in seconds, thereby exploring a new paradigm to sinter porous ceramics with limited coarsening. A range of porous ceramic SSEs (i.e., $\text{Li}_{6.5}\text{La}_3\text{Zr}_{1.5}\text{Ta}_{0.5}\text{O}_{12}$ (LLZTO), $\text{Li}_{1.3}\text{Al}_{0.3}\text{Ti}_{1.7}(\text{PO}_4)_3$ (LATP), and $\text{Li}_{0.3}\text{La}_{0.567}\text{TiO}_3$ (LLTO)) on various substrates (i.e., Al_2O_3 sheets, titanium (Ti), stainless steel, and carbon paper) are demonstrated using this method.

2. Results and Discussion

In a typical process, the precursor powders go through reactive sintering by Joule-heated carbon strips at 1273 K to form desired phase, meanwhile the pores are created and preserved due to the short sintering duration (Figure 1A). Owing to the fast ramping and quenching rates ($10^2\text{--}10^3\text{ K s}^{-1}$) of the heater, the whole sintering process can be completed within 10 s (compared to hours by conventional sintering). Pure crystalline phase and thus high ionic conductivity of the ceramic SSE can be achieved by the high temperature; meanwhile, the great tunability in sintering duration is critical to control the degree of densification toward the desired porous structure. The ultrafast sintering process is also effective in reducing the loss of volatile elements during sintering for a high material quality. Note that the size of carbon heater used in this approach is easily adjustable, which allows for good scalability of the 3D SSE scaffolds. This technique can be further integrated with a solution-based printing process to sinter 3D SSE scaffolds as thin and

flexible films. As a proof-of-concept, a porous LLZTO (denoted as P-LLZTO) membrane with a size of 10 cm^2 and a thickness of $20\text{ }\mu\text{m}$ is demonstrated. Macroscopically, the membrane is highly uniform throughout the whole substrate (Figure 1B). Microscopically, the grains partially fuse together to create a porous and integrated structure (Figure 1C).

To print the LLZTO powder precursors for sintering, we use an airbrush to spray a thin layer with a thickness of $10\text{--}100\text{ }\mu\text{m}$ on a substrate. The spraying process can be conducted on a range of substrates such as metal foils and ceramic sheets (Figure S1, Supporting Information). Using an electrified carbon heater with accurately controlled electrical current, we sintered the precursor layer at 1273 K in argon for only $\approx 10\text{ s}$ (Figure 2A). The contour image indicates uniform temperature distribution across the carbon heater as well as the sample for the optimal sintering result. Using scanning electron microscopy (SEM), we characterized the morphology of the sintered P-LLZTO layer supported on an Al_2O_3 substrate. Cross-sectional SEM image shows a flat and crack-free P-LLZTO layer with thickness of $\approx 12\text{ }\mu\text{m}$ (Figure 2B). Through gradually enlarging the magnification, the uniformly distributed pores and neck growth between grains can be clearly observed (Figure 2C,D). The elemental mapping by energy-dispersive X-ray spectroscopy (EDS) shows no cross-diffusion between the SSE layer and the Al_2O_3 substrate (Figure 2E). The LLZTO precursor layer was also sintered using a conventional furnace for 1 min at 1273 K as a control, which creates similar porous structure (Figure S2, Supporting Information). However, X-ray diffraction (XRD) shows that the control sample exhibits impurity phases (i.e., $\text{La}_2\text{Zr}_2\text{O}_7$) due to severe Li loss by the long ramping and cooling process ($\approx 5\text{ h}$) (Figure 2F). In contrast, our method formed the desired cubic garnet phase with high purity. Furthermore,

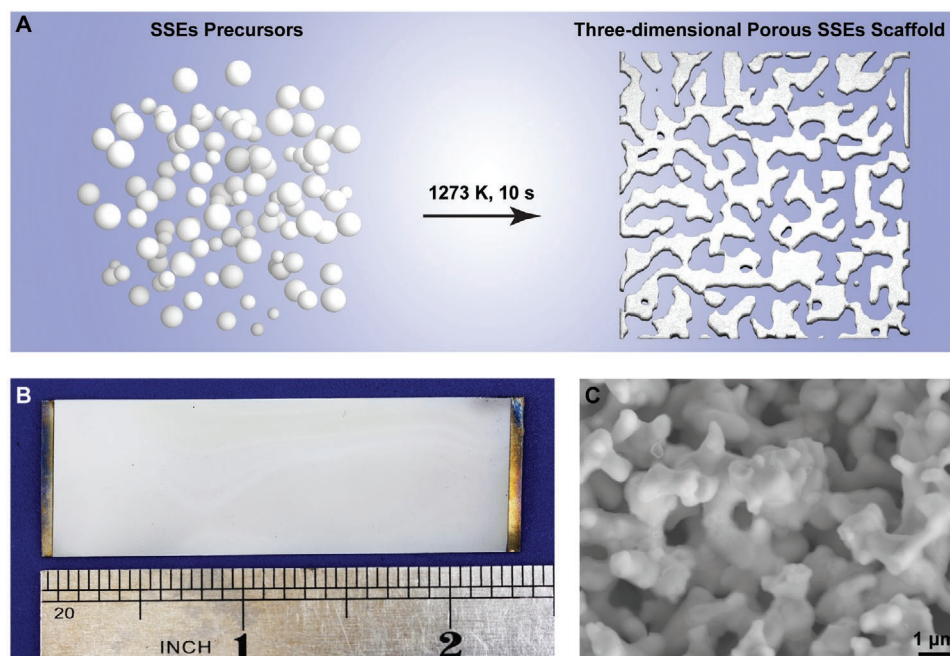


Figure 1. Schematic of the 3D porous SSE scaffolds. A) Transformation of precursor powders to 3D porous SSE scaffolds at 1273 K for 10 s by our ultra-fast sintering technique. B) Digital image of the P-LLZTO membrane supported on the stainless-steel foil substrate with dimensions of $5 \times 2 \times 0.002\text{ cm}$. C) Microstructure of the P-LLZTO membrane, showcasing neck growth between grains and uniformly distributed pores.

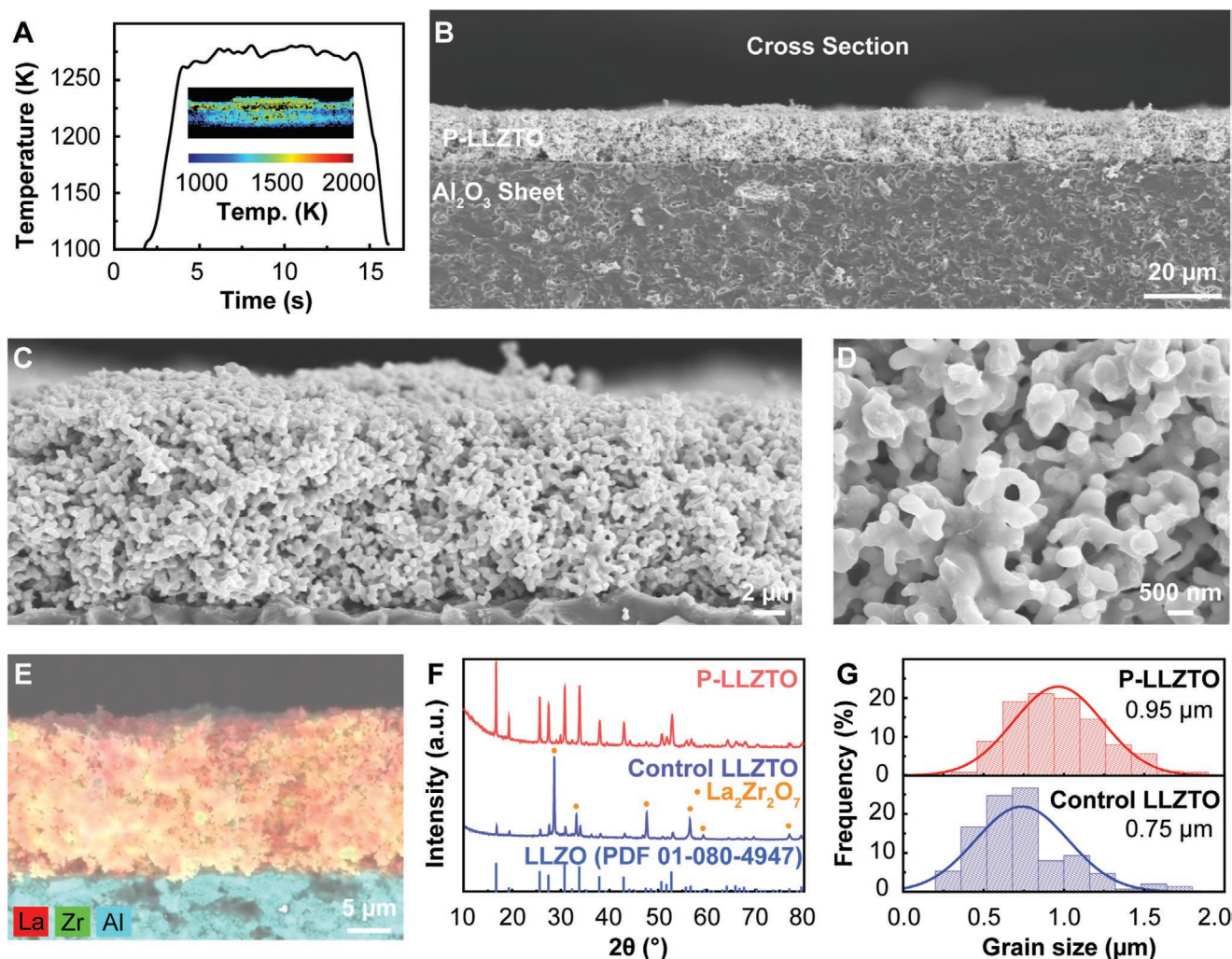


Figure 2. Characterization of the P-LLZTO. A) Temperature profile of the carbon heater during the ultrafast sintering process. The inset shows the uniform temperature distribution of the sample on the carbon heater. B) SEM image of the P-LLZTO layer supported on the Al₂O₃ substrate, showcasing a uniform, crack-free, and porous membrane. C,D) Zoom-in SEM images of the P-LLZTO layer, showcasing the neck growth between grains and porous structure. E) EDS mapping of P-LLZTO membranes on the Al₂O₃ substrate with minimal cross-diffusion. F) XRD pattern of the P-LLZTO and control sample. G) Histograms of grain size distribution for the P-LLZTO and control sample.

the grain size of the control sample is smaller than that of the P-LLZTO sintered by our method, which may be ascribed to the low temperature and severe Li loss during sintering.^[37] These results indicate that our rapid sintering technique is more effective in forming desired phases while maintaining the continuous porous structure.

To better understand the formation of porous structure, we sintered a series of LLZTO with various microstructure using temperatures from 1073 to 1773 K and sintering durations from 3 to 10 s. The LLZTO layers were sintered on the transparent MgO single crystal substrate to better observe their appearance changes (Figure 3A). The white LLZTO precursors (Figure S3, Supporting Information) transitioned from gray to white and then to transparent with temperature increased from 1073 to 1773 K. Note that the sample sintered at 1073 K for 10 s turned into a grayish color, likely due to the residue of the carbonization of poly(vinylpyrrolidone) (PVP). As temperature increased from 1073 to 1773 K, the layer became denser and denser due to the

growth and merging of grains, with thickness decreased from 14 to 8 μm (Figure 3B). The sample sintered at 1073 K for 10 s is still mainly composed by precursor powders without being fully reacted (Figure 3C). In contrast, the layer sintered at 1273 K for 10 s exhibits neck growth between grains, forming a 3D porous scaffold (P-LLZTO). Due to the diffraction of light, it macroscopically shows an opaque white color (Figure S4, Supporting Information). Further increasing the sintering temperature to 1773 K induces densification and grain growth to destroy the porous structure, despite of reducing the sintering duration from 10 to 3 s. The XRD pattern of the precursors sintered at 1073 K for 10 s does not match the cubic garnet peaks (PDF 01080 4947), while those of the precursors sintered at 1273 K for 10 s and at 1773 K for 3 s show the desired phase (Figure 3D). In comparison, the layer sintered at 1773 K for 10 s shows La₂Zr₂O₇ phase instead of the desired cubic garnet phase, likely due to the severe Li loss. We tested the total ionic conductivity of the formed LLZTO layers by electrochemical impedance

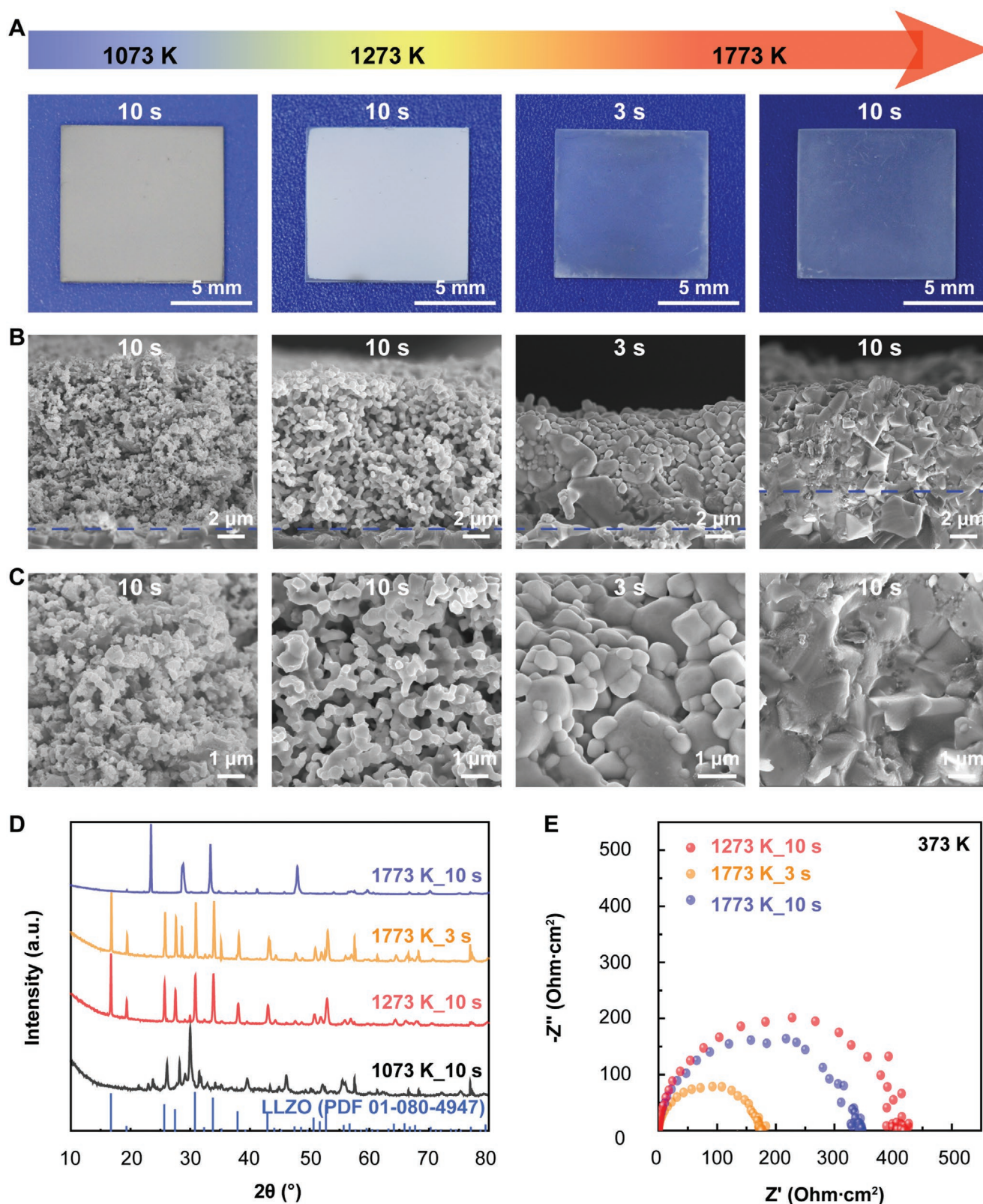


Figure 3. Characterization of the LLZTO layer sintered at different conditions. A) Digital images of a series of LLZTO layers sintered from 1073 to 1773 K. B) SEM images of LLZTO layers sintered from 1073 to 1773 K. C) High-magnification SEM images of LLZTO layers sintered from 1073 to 1773 K. D) XRD patterns of LLZTO layers sintered from 1073 to 1773 K. E) Nyquist plots of the Li/LLZTO membranes/Li symmetrical cells using LLZTO layers sintered at 1273 and 1773 K. The EIS curves were collected at 373 K.

spectroscopy (EIS) at 373 K using in-plane LiSn alloy electrodes (Figure 3E and Figure S5, Supporting Information). The P-LLZTO membrane (sintered at 1273 K for 10 s) shows a good total ionic conductivity of $\approx 7.3 \times 10^{-4} \text{ S cm}^{-1}$ at 373 K, which confirms the continuous Li-ion pathways. Compared with conventional furnace sintering as a control as well as with the literature,^[31,32] the P-LLZTO membrane sintered by our ultrafast method shows much better tortuosity and well-established neck growth between grains.

To demonstrate the universality of this method, we sintered another two porous SSEs using the same process: LATP and LLTO. The sintered porous LATP layer is flat and crack-free, showcasing a thickness of $\approx 13 \mu\text{m}$ (Figure 4A). Its XRD pattern agrees with the LATP phase (PDF 350754) after subtracting the diffraction peaks from the Al_2O_3 substrate (PDF 100173) (Figure 4B). The sintered grains and 3D porous scaffold can be clearly observed while gradually zooming in under SEM (Figure 4C,D). We use EDS mapping to characterize the elemental distribution of the Al_2O_3 -supported LATP layer, which showed no cross-diffusion (Figure 4E). Similar to LATP, we also synthesized porous LLTO 3D scaffold with a thickness of $\approx 6 \mu\text{m}$ (Figure 4F). The LLTO also exhibits highly crystalline phase by XRD (Figure 4G) as well as the desired porous structure by high-magnification SEM (Figure 4H,I). No phase segregation or cross-diffusion occurred between the porous LLTO and the Al_2O_3 substrate by EDS mapping (Figure 4J). These results strongly indicate that our method is a general approach to create 3D porous SSE scaffold for a range of ceramic Li-ion conductors.

In addition to the universality of SSEs, our method also allows for the use of various substrate materials owing to the relatively low sintering temperature needed for the 3D porous scaffold. Using LLZTO as a model SSE material, we sinter P-LLZTO on a Ti foil (Figure 5A), a stainless-steel foil (Figure 5B), and a carbon paper (Figure 5C) to demonstrate the broad utility of our approach. The porous nature and thinness of these P-LLZTO layers allow for the bending of the substrate, which potentially enables flexible battery applications. We further demonstrate a composite SSE based on our 3D porous SSE scaffold by impregnating stainless-steel-supported P-LLZTO with poly(ethylene oxide) (PEO) and lithium bis(trifluoromethanesulfonyl)imide (LiTFSI) salt. From both top-view (Figure 5D) and cross-sectional views (Figure 5E,F), a dense microstructure can be confirmed where PEO completely filled the pores with good interfacial wetting to LLZTO. Compared with the Fourier transform infrared (FTIR) spectra of PEO with LiTFSI (Figure 5G), the intensity of $-\text{CH}_2$ wagging (842 cm^{-1}) and twisting (951 cm^{-1}) bands on the composite SSE FTIR spectra significantly decreased, indicating that the crystallization of PEO was impeded after being integrated into the P-LLZTO scaffold.^[38,39] Moreover, no diffraction peaks of PEO can be observed for the composite SSE by XRD (Figure S6, Supporting Information), suggesting its amorphous state. By measuring EIS of the stainless-steel/composite electrolyte/stainless-steel symmetrical cell (Figure 5H), the ionic conductivity at room temperature is calculated to be $\approx 1.9 \times 10^{-4} \text{ S cm}^{-1}$. Varying the temperature from 298 to 333 K gradually decreases the impedance as reflected on the Nyquist plot (Figure 5I). By fitting the

Arrhenius relationship, an activation energy of 0.39 eV can be calculated, which is one of the best values among literature reports.^[40,41] The EIS of Ti foil/composite electrolyte/Ti foil symmetrical cell (Figure S7, Supporting Information) was also tested, which demonstrates a total ionic conductivity of $\approx 1.2 \times 10^{-4} \text{ S cm}^{-1}$ at 298 K.

3. Conclusion

We have developed a facile yet effective method to sinter 3D porous SSE scaffolds. The method is based on Joule heating of carbon heaters for reactive sintering of SSE precursors at a high temperature in seconds. Through accurately controlling the sintering temperature and duration, both pure crystalline phase and desired porous structure can be obtained. Our approach is generally applicable to a number of ceramic SSEs (e.g., LLZTO, LATP, and LLTO) on a range of substrates (e.g., Al_2O_3 sheet, Ti, stainless steel, and carbon paper). The thin and porous structure allows for potential application in flexible batteries. Using LLZTO as a model SSE material, we demonstrate a composite SSE by infiltrating PEO with LiTFSI salt into the porous scaffold. A high ionic conductivity of $1.9 \times 10^{-4} \text{ S cm}^{-1}$ at room temperature is achieved due to the continuous Li-ion pathways of the P-LLZTO scaffold and the well-wetted P-LLZTO/PEO interface. This method offers a new route toward constructing a range of 3D scaffolds with SSEs for all-solid-state battery applications.

4. Experimental Section

Preparation of the LLZTO Precursors: LLZTO powder precursors were prepared by mixing Li_2CO_3 (99.9%, Sigma Aldrich), La_2O_3 (99.9%, Sigma Aldrich), ZrO_2 (99.9%, Sigma Aldrich), and Ta_2O_5 (99.9%, Sigma Aldrich) powders in a stoichiometric ratio with 10 wt% excessive Li_2CO_3 . The powder mixture was then ball milled at 400 rpm in isopropyl alcohol for 6 h, followed by drying at 80°C overnight before using.

Preparation of the LATP Precursors: LATP powder precursors including Li_2CO_3 (additional 10 wt% Li_2CO_3 was added), Al_2O_3 (99.9%, Sigma Aldrich), TiO_2 (99.9%, Sigma Aldrich), and $\text{NH}_4\text{H}_2\text{PO}_4$ (99.9%, Sigma Aldrich) powders were stoichiometrically mixed, then ball milled and dried using the same process for LLZTO.

Preparation of the LLTO Precursors: LLTO powder precursors including Li_2CO_3 (additional 10 wt% Li_2CO_3 was required), La_2O_3 , and TiO_2 powders were stoichiometrically mixed, then ball milled and dried using the same process for LLZTO.

Preparation of the Porous SSE Scaffolds: The precursor solution was prepared by dispersing precursor powders and 5 wt% PVP as binder in ethanol with a concentration of 20 mg mL^{-1} under ultrasonication. Then the precursor solution was printed on the substrates (heated on 180°C) with a gap of 2 cm by using airbrush set (Point Zero). Finally, the printed membranes were sintered on carbon heater (AvCarb Felt G200) in an argon atmosphere within 20 s. The temperature was varied by adjusting the input current of DC power supply (Volteq HY6020EX).

Preparation of the PEO/P-LLZTO Composite SSE: PEO ($M_w = 600,000 \text{ g mol}^{-1}$, Sigma Aldrich) and LiTFSI salt (99.9%, Sigma Aldrich) were mixed in acetonitrile (99.9%, Sigma Aldrich) with a EO:Li ratio of 10:1. Then the homogeneous solution was impregnated into the sintered P-LLZTO scaffold by drop-casting. The prepared composite SSE was dried at 65°C for 24 h in an argon-filled glovebox to remove the solvent.

Characterization: The morphology and EDS mapping were conducted on Hitachi SU-70 SEM instrument. The crystalline structure was

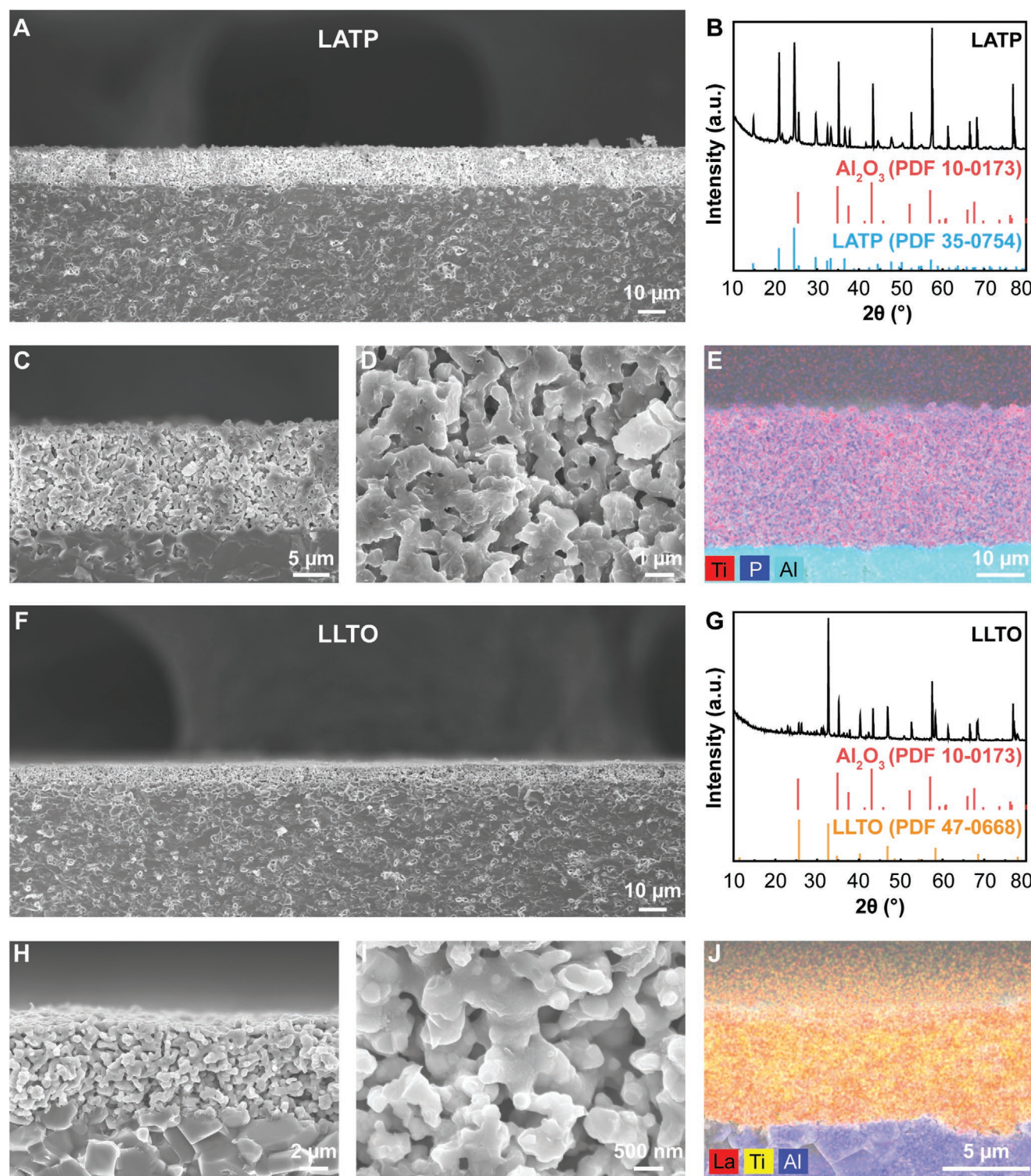


Figure 4. Synthesizing other porous SSEs. A) SEM image of the porous LATP layer with a thickness of $\approx 13\ \mu\text{m}$ supported on a Al_2O_3 substrate. B) XRD pattern of the porous LATP. C,D) Zoom-in SEM images of the porous LATP. E) EDS mapping of the porous LATP supported on a Al_2O_3 substrate. F) SEM image of the porous LLTO layer with a thickness of $\approx 6\ \mu\text{m}$ supported on a Al_2O_3 substrate. G) XRD pattern of the porous LLTO. H,I) High-magnification SEM images of the porous LLTO. J) EDS mapping of the porous LLTO supported on a Al_2O_3 substrate.

measured using the Bruker D8 Advance diffractometer with $\text{Cu K}\alpha$ radiation. The FTIR was carried out using the Nicolet iS10 spectrometer. The sintering temperature of carbon heater was measured using a

high-speed camera (Phantom Miro M110) as described in our previous work.^[36] The EIS spectra were collected using a potentiostat (BioLogic MPG-2) with a frequency range from 100 mHz to 1 MHz.

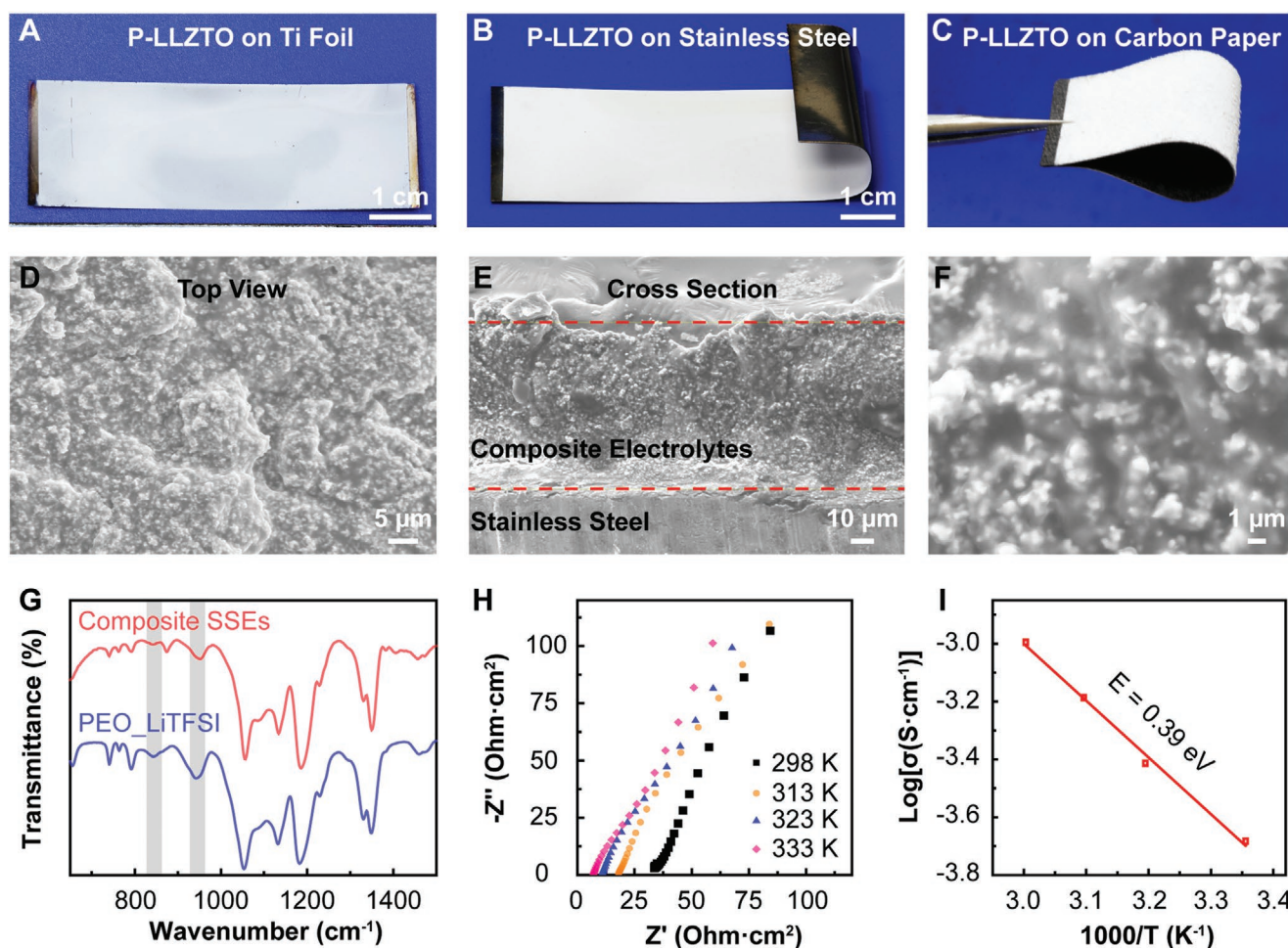


Figure 5. P-LLZTO on various substrates and P-LLZTO with PEO. A–C) P-LLZTO sintered on a Ti foil, a stainless-steel foil and a carbon paper, respectively. D) SEM image of the composite electrolyte containing the 3D P-LLZTO scaffold and PEO with LiTFSI salt. E) Cross-sectional SEM image of the composite electrolyte. F) Zoom-in SEM image of the composite electrolyte. G) FTIR spectra of the composite electrolyte and PEO with LiTFSI salt. H) Nyquist plots of the stainless-steel/composite electrolyte/stainless-steel symmetrical cell with temperature ranging from 298 to 333 K. I) Arrhenius relationship of the composite electrolyte, showing an activation energy of 0.39 eV.

Supporting Information

Supporting Information is available from the Wiley Online Library or from the author.

Acknowledgements

The authors acknowledge the support from the University of Maryland A. James Clark School of Engineering. The authors acknowledge the Maryland Nanocenter and Advanced Imaging and Microscopy (AIM) Lab. The authors thank Dylan Kline and Michael R. Zachariah for their help on the temperature measurement.

Conflict of Interest

The authors declare no conflict of interest.

Author Contributions

R.W., Q.D., and C.W. contributed equally to this work. L.H., R.W., C.W., and Q.D. designed the experiments. R.W., C.W., and W.P. performed

the sintering experiments. R.W. and M.G. carried out the SEM characterization. R.W., M.H., and J.G. measured the electrochemical properties. J.G. created the schematic illustrations and helped collect the digital images. R.W. and H.X. prepared the composite electrolytes. X.W. measured the sintering temperature. S.H. conducted the FTIR test. L.H., J.L., R.W., and Q.D. collectively wrote the paper. All authors commented on the final manuscript.

Data Availability Statement

The data that support the findings of this study are available from the corresponding author upon reasonable request.

Keywords

composite electrolytes, high-temperature sintering, porous scaffolds, solid-state electrolytes, ultrafast sintering

Received: January 27, 2021

Revised: April 23, 2021

Published online: July 19, 2021

- [1] Y. Xiao, Y. Wang, S.-H. Bo, J. C. Kim, L. J. Miara, G. Ceder, *Nat. Rev. Mater.* **2019**, 5, 105.
- [2] Y. Liu, B. Xu, W. Zhang, L. Li, Y. Lin, C. Nan, *Small* **2020**, 16, 1902813.
- [3] Y. Jin, K. Liu, J. Lang, D. Zhuo, Z. Huang, C.-a. Wang, H. Wu, Y. Cui, *Nat. Energy* **2018**, 3, 732.
- [4] A. J. Samson, K. Hofstetter, S. Bag, V. Thangadurai, *Energy Environ. Sci.* **2019**, 12, 2957.
- [5] D. H. Liu, Z. Bai, M. Li, A. Yu, D. Luo, W. Liu, L. Yang, J. Lu, K. Amine, Z. Chen, *Chem. Soc. Rev.* **2020**, 49, 5407.
- [6] J. Zhang, N. Zhao, M. Zhang, Y. Li, P. K. Chu, X. Guo, Z. Di, X. Wang, H. Li, *Nano Energy* **2016**, 28, 447.
- [7] R. Chen, Q. Li, X. Yu, L. Chen, H. Li, *Chem. Rev.* **2020**, 120, 6820.
- [8] A. Manthiram, X. Yu, S. Wang, *Nat. Rev. Mater.* **2017**, 2, 16103.
- [9] F. Zhou, Z. Li, Y. Y. Lu, B. Shen, Y. Guan, X. X. Wang, Y. C. Yin, B. S. Zhu, L. L. Lu, Y. Ni, Y. Cui, H. B. Yao, S. H. Yu, *Nat. Commun.* **2019**, 10, 2482.
- [10] J. C. Bachman, S. Muy, A. Grimaud, H.-H. Chang, N. Pour, S. F. Lux, O. Paschos, F. Maglia, S. Lupart, P. Lamp, L. Giordano, Y. Shao-Horn, *Chem. Rev.* **2016**, 116, 140.
- [11] J. Y. Liang, X. D. Zhang, X. X. Zeng, M. Yan, Y. X. Yin, S. Xin, W. P. Wang, X. W. Wu, J. L. Shi, L. J. Wan, Y. G. Guo, *Angew. Chem., Int. Ed.* **2020**, 59, 6585.
- [12] J. Wan, J. Xie, X. Kong, Z. Liu, K. Liu, F. Shi, A. Pei, H. Chen, W. Chen, J. Chen, X. Zhang, L. Zong, J. Wang, L. Q. Chen, J. Qin, Y. Cui, *Nat. Nanotechnol.* **2019**, 14, 705.
- [13] F. C. Giovanni Battista Appetecchi, P. Romagnoli, B. Scrosati, U. Heider, R. Oesten, *Electrochem. Commun.* **1999**, 1, 83.
- [14] A. Gupta, E. Kazyak, N. P. Dasgupta, J. Sakamoto, *J. Power Sources* **2020**, 474, 228598.
- [15] Q. Zhao, X. Liu, S. Stalin, K. Khan, L. A. Archer, *Nat. Energy* **2019**, 4, 365.
- [16] H. Huo, Y. Chen, J. Luo, X. Yang, X. Guo, X. Sun, *Adv. Eng. Mater.* **2019**, 9, 1804004.
- [17] C. Wang, K. Fu, S. P. Kammampata, D. W. McOwen, A. J. Samson, L. Zhang, G. T. Hitz, A. M. Nolan, E. D. Wachsman, Y. Mo, V. Thangadurai, L. Hu, *Chem. Rev.* **2020**, 120, 4257.
- [18] R. Murugan, V. Thangadurai, W. Weppner, *Angew. Chem., Int. Ed.* **2007**, 46, 7778.
- [19] N. Kamaya, K. Homma, Y. Yamakawa, M. Hirayama, R. Kanno, M. Yonemura, T. Kamiyama, Y. Kato, S. Hama, K. Kawamoto, A. Mitsui, *Nat. Mater.* **2011**, 10, 682.
- [20] T. Famprikis, P. Canepa, J. A. Dawson, M. S. Islam, C. Masquelier, *Nat. Mater.* **2019**, 18, 1278.
- [21] T. Krauskopf, F. H. Richter, W. G. Zeier, J. Janek, *Chem. Rev.* **2020**, 120, 7745.
- [22] X. Chen, W. He, L.-X. Ding, S. Wang, H. Wang, *Energy Environ. Sci.* **2019**, 12, 938.
- [23] S. Bag, C. Zhou, P. J. Kim, V. G. Pol, V. Thangadurai, *Energy Storage Mater.* **2020**, 24, 198.
- [24] W. Liu, N. Liu, J. Sun, P. C. Hsu, Y. Li, H. W. Lee, Y. Cui, *Nano Lett.* **2015**, 15, 2740.
- [25] W. Liu, D. Lin, J. Sun, G. Zhou, Y. Cui, *ACS Nano* **2016**, 10, 11407.
- [26] S. Zekoll, C. Marriner-Edwards, A. K. O. Hekselman, J. Kasemchainan, C. Kuss, D. E. J. Armstrong, D. Cai, R. J. Wallace, F. H. Richter, J. H. J. Thijssen, P. G. Bruce, *Energy Environ. Sci.* **2018**, 11, 185.
- [27] H. Xie, C. Yang, K. K. Fu, Y. Yao, F. Jiang, E. Hitz, B. Liu, S. Wang, L. Hu, *Adv. Eng. Mater.* **2018**, 8, 1703474.
- [28] K. Pan, L. Zhang, W. Qian, X. Wu, K. Dong, H. Zhang, S. Zhang, *Adv. Mater.* **2020**, 32, 2000399.
- [29] H. Shen, E. Yi, S. Heywood, D. Y. Parkinson, G. Chen, N. Tamura, S. Sofie, K. Chen, M. M. Doeff, *ACS Appl. Mater. Interfaces* **2020**, 12, 3494.
- [30] C. Yang, L. Zhang, B. Liu, S. Xu, T. Hamann, D. McOwen, J. Dai, W. Luo, Y. Gong, E. D. Wachsman, L. Hu, *Proc. Natl. Acad. Sci. USA* **2018**, 115, 3770.
- [31] Y. Ren, T. Liu, Y. Shen, Y. Lin, C.-W. Nan, *Ionics* **2017**, 23, 2521.
- [32] K. Fu, Y. Gong, G. T. Hitz, D. W. McOwen, Y. Li, S. Xu, Y. Wen, L. Zhang, C. Wang, G. Pastel, J. Dai, B. Liu, H. Xie, Y. Yao, E. D. Wachsman, L. Hu, *Energy Environ. Sci.* **2017**, 10, 1568.
- [33] S. Xu, D. W. McOwen, L. Zhang, G. T. Hitz, C. Wang, Z. Ma, C. Chen, W. Luo, J. Dai, Y. Kuang, E. M. Hitz, K. Fu, Y. Gong, E. D. Wachsman, L. Hu, *Energy Storage Mater.* **2018**, 15, 458.
- [34] L. Buannic, M. Navroij, S. M. Miller, J. Zagorski, K. T. Faber, A. Llordés, *J. Am. Ceram. Soc.* **2019**, 102, 1021.
- [35] S. Deville, E. Saiz, R. K. Nalla, A. P. Tomsia, *Science* **2006**, 311, 515.
- [36] C. Wang, W. Ping, Q. Bai, H. Cui, R. Hensleigh, R. Wang, A. H. Brozena, Z. Xu, J. Dai, Y. Pei, C. Zheng, G. Pastel, J. Gao, X. Wang, H. Wang, J. C. Zhao, B. Yang, X. R. Zheng, J. Luo, Y. Mo, B. Dunn, L. Hu, *Science* **2020**, 368, 521.
- [37] X. Huang, Y. Lu, Z. Song, K. Rui, Q. Wang, T. Xiu, M. E. Badding, Z. Wen, *Energy Storage Mater.* **2019**, 22, 207.
- [38] H. Zhuang, W. Ma, J. Xie, X. Liu, B. Li, Y. Jiang, S. Huang, Z. Chen, B. Zhao, *J. Alloys Compd.* **2020**, 860, 157915.
- [39] F. Chen, D. Yang, W. Zha, B. Zhu, Y. Zhang, J. Li, Y. Gu, Q. Shen, L. Zhang, D. R. Sadoway, *Electrochim. Acta* **2017**, 258, 1106.
- [40] W. Zha, F. Chen, D. Yang, Q. Shen, L. Zhang, *J. Power Sources* **2018**, 397, 87.
- [41] Z. Wan, D. Lei, W. Yang, C. Liu, K. Shi, X. Hao, L. Shen, W. Lv, B. Li, Q.-H. Yang, F. Kang, Y.-B. He, *Adv. Funct. Mater.* **2019**, 29, 1805301.